https://doi.org/10.5194/egusphere-2025-733
Preprint. Discussion started: 14 March 2025

Equilibrium-Approximated Solutions to the Reactive Lauwerier Problem: Thermal Fronts as Controls on Reactive Fronts in Earth Systems

Roi Roded

Civil, Environmental, and Geo-Engineering, University of Minnesota Twin Cities, Minneapolis, MN, USA

Correspondence to: R. Roded (roi.roded@mail.huji.ac.il)

Abstract

Rates of subsurface rock alteration by reactive flows are often essentially independent of kinetic rates and governed solely by solute transport to and from reactive mineral surfaces. This allows for a major simplification, making models tractable in complex kinetic systems through the widely applied local equilibrium assumption. Here, this assumption is applied to the Reactive Lauwerier Problem (RLP), which describes non-isothermal fluid injection into a confined aquifer, driving thermally induced solubility changes and reactions. Specifically, depending on the solubility nature of a given mineral, the thermally induced solubility changes can lead to either undersaturation and dissolution or supersaturation and precipitation. Using this framework, solutions for reaction rate and porosity evolution are developed and analyzed, leading to a functional time-dependent criterion that incorporates thermal parameters. A key feature—coalescence of thermal and reactive fronts—is then analyzed under various conditions. Finally, the applicability of the equilibrium model for important fluid-rock interaction processes is then discussed and examined, including sedimentary reservoir development, mineral carbonation in peridotite, and ore deposit formation. The findings highlight that such thermally driven reactive fronts near equilibrium often become essentially stationary after a relatively short period. As a result, their spatial evolution is governed solely by geological processes operating on much longer timescales.

1. Introduction

Natural and anthropogenic systems are often complex, involving intricate interactions between various processes, which makes developing a mechanistic understanding of the system challenging. However, the disparity in timescales between these processes often allows for significant simplification, as one process typically serves as the rate-limiting step that controls the

https://doi.org/10.5194/egusphere-2025-733
Preprint. Discussion started: 14 March 2025

system overall evolution. This simplification, in turn, enables the recovery of the system mechanistic behavior. Such systems range from climate science, where atmospheric and oceanic processes interact and operate at different timescales (Vallis, 2017), to multi-step biochemical processes and enzyme kinetics (Cornish-Bowden, 2013), traffic flow analysis (Lighthill and Whitham, 1955), epidemiology and disease spread (Anderson, 1991), economics (Solow, 1956) and crystal growth (Mullins and Sekerka, 1963).

Similarly, in geothermal systems, hydro-thermo-chemical processes often involve complex interactions. In particular, geochemical kinetics can be highly intricate, involving multiple species and reactions of varying orders, which are influenced by flow and transport dynamics and thermal variations (Appelo and Postma, 2004; Kolditz et al., 2016; Phillips, 2009). This complexity hinders the understanding of system behaviors and their description using tractable models. However, in many cases, the rate of transport is much slower than the reaction kinetics, effectively controlling the overall reaction rate. These conditions, known as transport-controlled, occur when the transport of reactants or reaction products dictates the reaction rate (Deng et al., 2016; Roded et al., 2020; Steefel and Maher, 2009).

Under transport-controlled conditions, the characteristic timescale of transport, t_A, is much larger than that of the reaction, t_R, ($t_A >> t_R$) and the system is close to chemical equilibrium (i.e., quasi-equilibrium). In such cases, the local equilibrium assumption is often invoked, and the assumption that the reaction rate depends solely on transport allowing to greatly simplify models (Andre and Rajaram, 2005; Lichtner et al., 1996; Molins and Knabner, 2019). The validity of the equilibrium model is determined by a large timescale ratio and the Damköhler number, *Da*, given by

$$Da = \frac{t_A}{t_R} = \frac{lA_s\lambda}{u_A} > 1, \quad (1)$$

where l is a local characteristic length scale, u_A denotes characteristic Darcy flux [L T^{-1}], A_s is the specific reactive area (L^2 to L^{-3} of porous medium) and λ is the kinetic reaction rate coefficient [L T^{-1}] (Lichtner et al., 1996; MacQuarrie and Mayer, 2005; Appendix A provides simple derivation of the condition in Eq. 1 for the thermally-driven reactive transport conditions considered in this study).

https://doi.org/10.5194/egusphere-2025-733
Preprint. Discussion started: 14 March 2025

Here, in this study, equilibrium model solutions for geothermal systems are derived, building on previous work (Roded et al., 2024b), in which thermally driven reactive transport solutions were developed within the framework of the *Lauwerier solution* (Lauwerier, 1955). The Lauwerier solution provides an analytical prediction of the thermal field development resulting from the injection of hot (or cold) fluid into a thin, non-reactive, confined layer system (Lauwerier, 1955; Stauffer et al., 2014).

The thermally-driven reactive transport solutions developed by Roded et al. (2024b) integrate temperature-dependent solubility into a reactive flow formulation while incorporating the thermal field based on the Lauwerier solution. Specifically, this setting, referred to as the Reactive Lauwerier Problem (RLP), accounts for thermal variations that drive the system out of geochemical equilibrium, thereby triggering chemical reactions. These disturbances stem from shifts in mineral solubility within groundwater, where thermal fluctuations can induce conditions of either supersaturation or undersaturation. Over time, these thermally-driven reactions lead to changes in rock porosity due to the precipitation, dissolution, or replacement of solid minerals and the associated volumetric changes (Phillips, 2009; Woods, 2015).

Depending on the natural solubility of the minerals in the system, an increase in temperature can lead to either dissolution or precipitation. This occurs because mineral solubilities can either decrease with temperature (*retrograde solubility*) or increase with it (*prograde solubility*; Jamtveit and Yardley, 1996; Phillips, 2009). A notable example includes the prograde solubility of silica, which commonly precipitates in geothermal systems from the cooling of fluids (Pandey et al., 2018; Rawal and Ghassemi, 2014; Taron and Elsworth, 2009). In contrast, carbonate minerals such as calcite and dolomite exhibit an inverse relationship with temperature and retrograde solubility, which is often pronounced and influenced by CO_2 concentration. Depending on the conditions, either rapid dissolution or rapid precipitation can occur in the case of common carbonate minerals (Andre and Rajaram, 2005; Coudrain-Ribstein et al., 1998).

Fluid recharge or injection under constrained physical and chemical conditions, as in RLP settings, is common in both natural and engineered geothermal systems and aquifers (Hidalgo et al., 2012; Phillips, 2009; Stauffer et al., 2014). These include mineral carbonation in ultramafic rocks (Kelemen et al., 2019; Roded and Dalton, 2024) and ore deposit formation by hydrothermal flows (Ingebritsen & Appold, 2012), aquifer thermal storage, pumping or reinjection of geothermal

https://doi.org/10.5194/egusphere-2025-733
Preprint. Discussion started: 14 March 2025

water, and groundwater storage and recovery applications (Diaz et al., 2016; Fleuchaus et al., 2018; Maliva, 2019).

In this study, equilibrium-approximated solutions for the RLP are first derived for radial and planar flows. Next, these solutions are compared to the reference solutions from Roded et al. (2024b) to validate them and discuss their limitations, along with the derivation of specific criteria for the RLP setup. Then, the evolution of reactive fronts under quasi-equilibrium conditions is analyzed for different scenarios. Interestingly, it is shown that under certain conditions, thermally driven reactive fronts cease to expand and become essentially stationary after a short timescale, remaining controlled by longer-term tectonic processes. This phenomenon is discussed in the context of key relevant processes, including the alteration of sedimentary aquifers, mineral carbonation, and the formation of ore deposits.

2. Settings and Model Equations

2.1. The Reactive Lauwerier Scenario

The Lauwerier problem describes the injection of a hot or cold fluid into a confined aquifer bounded by impermeable bedrock and caprock (Lauwerier, 1955; Stauffer et al., 2014). The fluid flows horizontally along the ξ coordinate, which can represent either the radial distance (r) in an axisymmetric configuration or the Cartesian coordinate (x), i.e., $\xi = r$ or x. A schematic representation of this system is provided in Fig. 1, with the nomenclature summarized in Appendix D.

Along the flow path downstream from the injection well, heat is transferred between the aquifer and the confining aquiclude layers, which conduct the heat. Within the aquifer, thermal variations influence mineral solubility (i.e., saturation concentration, $c_s(T)$). These solubility changes, in turn, lead to undersaturation and dissolution reactions or, conversely, to supersaturation and precipitation reactions, which modify the aquifer porosity (θ). Whether the porosity decreases or increases, and the magnitude of these changes, depends on both the temperature difference between the injected fluid and ambient conditions, and the solubility characteristics of the minerals involved (i.e., prograde or retrograde behavior). As mentioned in the Introduction, this work further examines conditions where reaction kinetics are fast and the Damköhler number is large ($Da > 1$).

https://doi.org/10.5194/egusphere-2025-733
Preprint. Discussion started: 14 March 2025

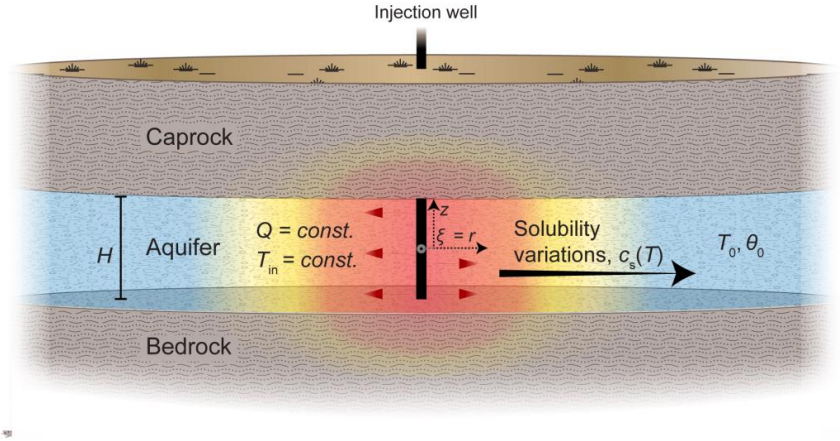

Figure 1. Outline of the Reactive Lauwerier Problem (RLP) for thermally driven reactive transport in geothermal systems. Hot (or cold) fluid is injected into an aquifer, confined between impermeable bedrock and caprock, at a steady flow rate, Q, and temperature, T_{in}. The initial temperature is T_0 and the aquifer thickness is H. Along the flow path downstream, heat from the aquifer conducts through the confining layers. The resulting thermal variations (depicted by color gradients) alter mineral solubility, $c_s(T)$, driving the system out of equilibrium and triggering chemical reactions that modify the aquifer porosity from its initial value, θ_0. In this work, it is further assumed that the Damköhler number is large ($Da > 1$) and that the equilibrium assumption holds. The vertical coordinate is denoted by z, while the horizontal coordinate, ξ, represents either the radial coordinate, r, or the Cartesian coordinate, x (i.e., $\xi = r$ or x). The reference point for both ξ and z is located at the center of the injection well, which exhibits axial symmetry (as shown in the sketch) or planar symmetry when Cartesian geometry is assumed (modified after Roded et al. (2024b)).

In terms of geometry, the model considers two primary settings. The first is radial flow, which represents injection from a single well, or accounts for naturally focused flow of deep-origin through faulted or fractured rock, discharging into a shallower aquifer (Craw, 2000; Micklethwaite and Cox, 2006; Roded et al., 2013, 2023; Tripp and Vearncombe, 2004). The second is planar flow, which describes injection from a row of wells arranged in a straight-line configuration, as initially formulated by Lauwerier (1955).

https://doi.org/10.5194/egusphere-2025-733
Preprint. Discussion started: 14 March 2025

2.2. Main Model Assumptions

The RLP conceptual model of Fig. 1 is formulated using conservation equations for heat and reactive transport supplemented by initial and boundary conditions. The original thermal Lauwerier solution and the reactive Lauwerier solutions involve several simplifying assumptions. Here, the main ones are repeated below. For a more comprehensive overview of the assumptions, the reader is referred to Roded et al. (2024b).

Thermal assumptions include neglecting the initial geothermal gradient and assuming that the basal geothermal heat flow is small compared to the heat supplied by the injected fluid. The aquifer is also assumed to be situated at depth, preventing heat from being transferred to the surface; otherwise, there would be greater heat exchange between the aquifer and the caprock. This assumption also depends on the timescale of interest: the thermal front, which rises over time, may not extend to the surface on a short timescale. However, over a longer period, it may transfer heat to the surface, which can be calculated using the characteristic timescale of conduction t_C ($t_C = l_C^2/\alpha_b$, where l accounts for the characteristic length scales of conduction and α_b is the thermal diffusivity).

In the confining layers, heat is transferred solely through conduction in the vertical direction (z), while neglecting lateral (ζ) heat conduction. This assumption restricts the model applicability to cases with high injected fluid fluxes, where mild lateral temperature gradients evolve. To evaluate the validity of this assumption, a thermal Péclet number is employed, which compares heat advection in the aquifer to lateral heat conduction in the confirming layers: $Pe_T = u_A l/\alpha_b$, where l is a length scale at which substantial temperature variation occurs (e.g., larger than 2 % from the total temperature change, ΔT). *A posteriori* inspection confirms that $Pe_T >> 1$ at all times at the conditions considered here. Moreover, after the initial moments, the length scale l should exceed the vertical dimension of the aquifer, H, where complete thermal mixing is assumed ($l >> H$). This assumption may not hold if a thick aquifer (i.e., large H) is considered, and significant vertical temperature gradients are expected to develop.

Additionally, thermal and solute dispersions within the aquifer are neglected, as both thermal (Pe_T) and solute (Pe_s) Péclet numbers are assumed to be large. Properties of the fluid and solid phases, such as density and thermal conductivity, are assumed to be constant and temperature-independent.

https://doi.org/10.5194/egusphere-2025-733
Preprint. Discussion started: 14 March 2025

Last, it is assumed that $Da > 1$ and the equilibrium assumption is applied. As a result, reaction rates are independent of kinetics (λ) and the reactive surface area (A_s).

2.3. The Basic Conservation Equations

Here, the basic conservation equations are presented, simplified using the assumptions considered, and then used to develop equilibrium solutions. For a more comprehensive overview, more general versions of the conservation equations are provided in the Supplementary Material (SM). In what follows, the radial case ($\xi = r$) is considered first, followed by planar flow case and Cartesian coordinates ($\xi = x$).

Assuming that heat transfer in the radial direction, r, is negligible, the heat equation in the bedrock and caprock confining the aquifer is,

$$\frac{\partial T}{\partial t} = \alpha_{\mathrm{b}} \frac{\partial^2 T}{\partial z^2}, \quad \text{for} \quad \begin{cases} z \le -\dfrac{H}{2} \\ z \ge \dfrac{H}{2} \end{cases}, \tag{2}$$

where T denotes temperature, t is time, z is the vertical coordinate originating at the center of the injection well and H denotes the aquifer thickness (see Fig. 1). The thermal diffusivity is given by $\alpha_{\mathrm{b}} = K_{\mathrm{b}}/C\mathrm{p}_{\mathrm{b}}$, where the subscript b denotes bulk rock, K is the thermal conductivity, and Cp is the volumetric heat capacity (Chen and Reddell, 1983; Stauffer et al., 2014).

Assuming that heat transport in the aquifer is dominated by advection and that perfect mixing prevails in the transverse direction (z), a 'depth-averaged' heat transport equation can be derived for the aquifer domain:

$$C_{\mathrm{p_b}} H \frac{\partial T}{\partial t} = -C_{\mathrm{p_f}} H \frac{1}{r} \frac{\partial (ruT)}{\partial r} - \boldsymbol{n} \cdot \boldsymbol{\Theta}(r,t), \quad \text{for} \quad -\frac{H}{2} \le z \le \frac{H}{2}, \tag{3}$$

where subscript f denotes fluid and $u(r)$ is the Darcy flux, assumed to be uniform along the z direction and can be calculated from the total volumetric flow rate, Q, using $u = Q/(H2\pi r)$ (Andre and Rajaram, 2005; Lauwerier, 1955) . The $\boldsymbol{\Theta}$ function accounts for the heat exchange between the aquifer and the confining bedrock and caprock, calculated using Fourier's law, assuming continuous temperature at the interfaces:

https://doi.org/10.5194/egusphere-2025-733
Preprint. Discussion started: 14 March 2025

$$\boldsymbol{\Theta} = -2K_{\mathrm{b}} \frac{\partial T}{\partial z}\Big|_{z=\frac{H}{2},-\frac{H}{2}}. \tag{4}$$

The factor of two accounts for both the bedrock and caprock (Stauffer et al., 2014). In Eq. 3, ***n*** represents a unit vector directed outward from the aquifer and perpendicular to the interface between the aquifer and the bedrock or caprock. This orientation ensures that, e.g., in the case of a warmer aquifer, the upward and downward heat fluxes are negative.

The solute advection-reaction equation in the aquifer is:

$$0 = -u\frac{\partial c}{\partial r} - \Omega(r,t), \quad \text{for} \quad -\frac{H}{2} \leq z \leq \frac{H}{2}, \tag{5}$$

where c is the solute concentration [M L^{-3}] and Ω is the reaction rate (Chaudhuri et al., 2013; Szymczak and Ladd, 2012). Note that the transient and dispersivity terms in Eq. 5 are neglected, with the latter being omitted due to the assumption of $Pe_s >> 1$ (see SM). The justification for neglecting the transient term and invoking the quasi-static approximation in the derivation of Eq. 5, lies in the separation of timescales between the relaxation of solute concentration (t_A), heat conduction (t_C) in the confining rocks and mineral alteration (for in-depth analysis and discussion see Roded et al. (2024b) and as well, e.g., Bekri et al., 1995; Ladd and Szymczak, 2017; Lichtner, 1991; Roded et al., 2020).

Assuming a surface-controlled reaction and first-order kinetics, the reaction rate can be calculated using:

$$\Omega = A_s \lambda \Lambda, \tag{6}$$

where A_s is the specific reactive surface area (L^{-1}) and λ is the kinetic rate coefficient [L T^{-1}] (Dreybrodt et al., 2005; Steefel and Maher, 2009). Λ is defined here as the solute disequilibrium, comprising the difference between the concentration of dissolved ions and the saturation (equilibrium) concentration, c_s,

$$\Lambda = c - c_s(T). \tag{7}$$

Thus, the solute disequilibrium, Λ, is positive for supersaturation and negative for undersaturation. c_s is calculated as:

https://doi.org/10.5194/egusphere-2025-733
Preprint. Discussion started: 14 March 2025

$$c_s(T) = c_s(T_0) + \beta(T - T_0), \tag{8}$$

where T_0 denotes the initial temperature in the aquifer and the parameter $\beta = \partial c_s/\partial T$. In Eq. 8, a linear relation between c_s and T is assumed, with a constant proportionality factor β, which is positive for minerals of prograde solubility and negative for minerals of retrograde solubility (Corson and Pritchard, 2017; Woods, 2015).

Using the reaction rate from Eq. 6, the change in porosity, θ, can be calculated as:

$$\frac{\partial \theta}{\partial t} = -\frac{\Omega}{\nu c_{sol}}, \quad \text{for} \quad -\frac{H}{2} \le z \le \frac{H}{2}. \tag{9}$$

Here, c_{sol} represents the concentration of soluble solid mineral and ν accounts for the stoichiometry of the reaction. For planar flow and Cartesian coordinates, r can be substituted with x in the equations above, and Eq. 3 then takes the following form:

$$C_{p_b} H \frac{\partial T}{\partial t} = -u C_{p_f} H \frac{\partial T}{\partial x} - \boldsymbol{n} \cdot \boldsymbol{\Theta}(x,t), \quad \text{for} \quad -\frac{H}{2} \le z \le \frac{H}{2}. \tag{10}$$

2.4. Initial and Boundary Conditions

The initial conditions involve a uniform temperature, T_0, across the system. The boundary conditions at the injection well ($\xi = 0$) specify a constant rate of fluid injection at temperature T_{in}, with an initial solute disequilibrium of $\Lambda = 0$ (Eq. 7). It is assumed that the thickness of the bedrock and caprock, as well as the extent of the aquifer, are infinite.

3. Results: Equilibrium Solutions and Their Applicability

3.1. Derivation of the Equilibrium Solutions

3.1.1. Axisymmetric (Radial) Flow

Aquifer temperature. The solution for the temperature distribution in the aquifer (known as the Lauwerier solution) derived from solving Eqs. 2 and 3 for axisymmetry is given by:

$$T(r,t) = T_0 + \Delta T \operatorname{erfc}[\zeta(r,t) r^2], \tag{11}$$

where erfc is the complementary error function, $\Delta T = T_{in} - T_0$ is the difference between injection and ambient aquifer temperatures, and ζ is defined as:

https://doi.org/10.5194/egusphere-2025-733
Preprint. Discussion started: 14 March 2025

$$\zeta(r,t) = \frac{\pi\sqrt{K_b C_{p_b}}}{Q C_{p_f}\sqrt{t'}}. \quad (12)$$

The time variable is defined as $t' = t - 2rC_{p_b}/(C_{p_f}u)$, and the solution of Eq. 11 is valid when $t' > 0$ (Stauffer et al., 2014). Furthermore, it is assumed that a sufficiently long time has passed and that conditions satisfy $t' \approx t$ (for an analysis of the validity of this assumption, see Roded et al. (2024b)). Additionally, for simplicity, it is assumed that the heat capacities of both the confining rocks and the aquifer are identical. To account for non-uniform heat capacities, an alternative definition of Eq. 11 can be applied (see Eqs. 3.122 and 3.131, along with the corresponding definitions in Stauffer et al. (2014)).

Reactive solute transport. Rewriting Eq. 5 for the aquifer domain using the definition of Eq. 7 results in,

$$0 = -u\left[\frac{\partial \Lambda}{\partial r} + \frac{\partial c_s}{\partial r}\right] - \Omega(r,t). \quad (13)$$

Assuming instantaneous reaction and that quasi-equilibrium prevails, $\Lambda \approx 0$, so that Eq. 13 becomes,

$$\Omega = u\frac{\partial c_s(T)}{\partial r}. \quad (14)$$

The derivative $\partial c_s/\partial r$ can be obtained by differentiating the relationship given in Eq. 8, viz. $\partial c_s/\partial r = \beta \partial T/\partial r$, and by further substituting the Lauwerier solution (Eq. 11) and differentiating, which yields:

$$\frac{\beta \partial T}{\partial r} = -4\Delta T \frac{\beta \zeta r}{\sqrt{\pi}} e^{(-\zeta^2 r^4)}. \quad (15)$$

The solution for the reaction rate is thus given by:

$$\Omega(r,t) = -u4\Delta T \frac{\beta \zeta r}{\sqrt{\pi}} e^{(-\zeta^2 r^4)}. \quad (16)$$

https://doi.org/10.5194/egusphere-2025-733
Preprint. Discussion started: 14 March 2025

Substituting the solution for the reaction rate, Ω (Eq. 16), into Eq. 9 and integrating over time yields the solution for the porosity change:

$$\theta(r,t) = \theta_0 - 4u\Delta T \frac{\beta\zeta^2 r^3 t}{\upsilon c_{sol}\sqrt{\pi}} \Gamma\left(-\frac{1}{2}, \zeta^2 r^4\right), \tag{17}$$

where Γ is the incomplete gamma function.

3.1.2. Planar Flow

For the Cartesian case, with injection occurring along a line, the Lauwerier solution is:

$$T(x,t) = T_0 + \Delta T \mathrm{erfc}[\omega(x,t)x], \tag{18}$$

where ω is defined as:

$$\omega(x,t) = \frac{\sqrt{K_\mathrm{b} C_{\mathrm{p_b}}}}{H C_{\mathrm{p_f}} u\sqrt{t'}}, \tag{19}$$

and $t' = t - xC_{\mathrm{pb}}/(C_{\mathrm{pf}}u)$. Similarly to the radial case, the solution applies at sufficiently long times, where $t' \approx t$.

Following steps analogous to those in the radial case, the solutions are derived as:

$$\Omega(x,t) = -2u\Delta T \frac{\beta\omega}{\sqrt{\pi}} e^{(-\omega^2 x^2)}, \tag{20}$$

and

$$\theta(x,t) = \theta_0 - 2u\Delta T \frac{\beta\omega^2 xt}{\upsilon c_{sol}\sqrt{\pi}} \Gamma\left(-\frac{1}{2}, \omega^2 x^2\right). \tag{21}$$

3.2. Applicability of the Equilibrium Approximation

3.2.1. Comparison to the Reference Solution

In this section, the results of the equilibrium model solution for porosity are compared with more general solutions to the RLP, which will henceforth be referred to as the 'reference solutions.'

https://doi.org/10.5194/egusphere-2025-733
Preprint. Discussion started: 14 March 2025

These reference solutions account for far-from-equilibrium conditions and assume surface-controlled reactions and first-order kinetics. The case study considered in the comparison involves a typical scenario: dissolution of a fractured carbonate aquifer due to the injection of CO_2-rich hot water and cooling-driven calcite dissolution. First, the results presented by Roded et al. (2024b) for the reference solutions are briefly summarized to facilitate the comparison with the equilibrium solution. The reference solutions, along with the case study considered here, are detailed in Roded et al. (2024b). The reference solution equations are further provided in Appendix B, and the parameter values used are provided in Appendix C.

In Fig. 2, the results of CO_2-rich hot water injection at successive times since the beginning of the injection are shown (t = 0.2, 10 and 100 kyr). The Lauwerier solution and reference solutions are shown by continuous lines (Eqs. 11 and B.1-3), while the equilibrium solution for the porosity evolution is indicated by circle markers in Fig. 2c (Eq. 17). During the radial flow within the aquifer, the hot fluid cools by transferring heat into the confining layers, which heat up with time, resulting in the gradual advancement of the thermal front downstream (Fig. 2a). The cooling induces solute disequilibrium (Λ) associated with undersaturation (note that Λ is negative for undersaturation and positive for supersaturation, see Eq. 7). The magnitude of Λ in the aquifer is small compared to the absolute solubility change in the system, $\Delta c_s = |c_s(T_{in}) - c_s(T_0)|$, i.e., between $c_s(T_{in})$ at the injection point to $c_s(T_0)$ at ambient conditions ($|\Lambda|/\Delta c_s << 1\%$, see Fig. 2b). The small magnitude of disequilibrium is associated with relatively high PCO_2 considered (0.03 MPa) and rapid kinetics under these conditions.

Despite its small magnitude, the disequilibrium, Λ, governs the alteration of the aquifer and the evolution of its porosity. Notably, since the water at the inlet is hot and saturated with calcite, $c = c_s(T_{in})$, disequilibrium and the reaction rate are zero at the inlet, resulting in no change in porosity (see Fig. 2b and 3c, along with their magnified views). Disequilibrium (undersaturation) abruptly develops downstream of the injection well, initially forming a small minimum (at $r \approx 20$ m) before gradually diminishing to zero further downstream. In accordance with the disequilibrium, the porosity profile sharply increases near the inlet and then gradually decreases downstream (Fig. 2c). Undersaturation and dissolution along the flow path are governed by the interplay of three processes: (I) dissolution, which reduces undersaturation (bringing Λ closer to zero), (II) progressive cooling, which enhances undersaturation, and (III) advection, which transports

https://doi.org/10.5194/egusphere-2025-733
Preprint. Discussion started: 14 March 2025

reaction products (calcium ions) radially outward from the well, sustaining undersaturation. Here, fluid velocity and advection decay with a distance, following a $1/r$ relationship.

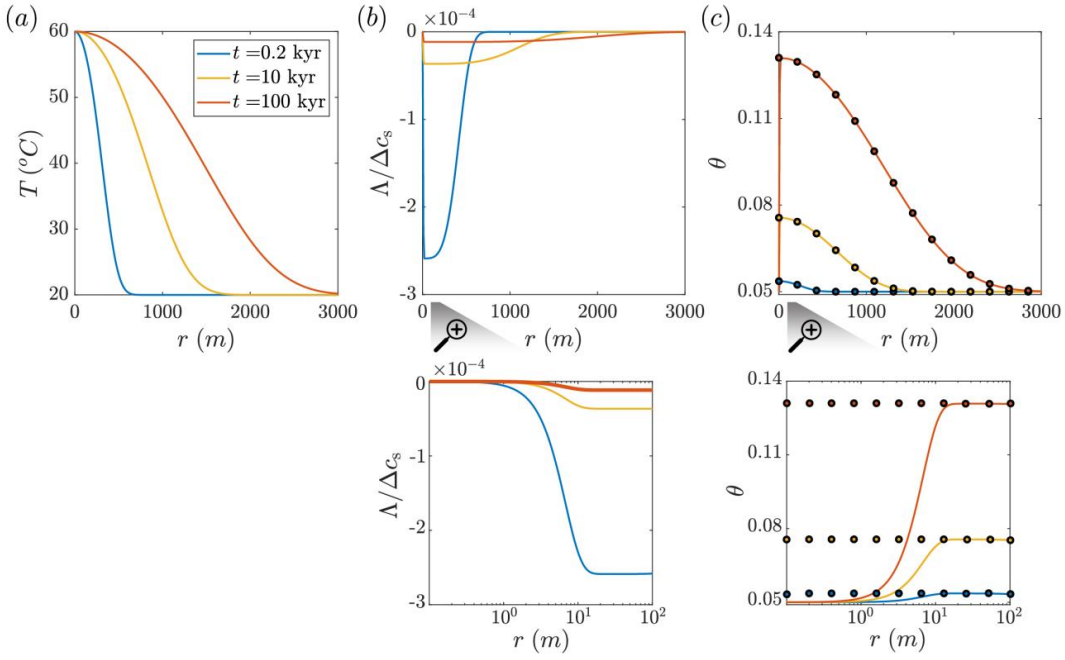

Figure 2. Comparison between the reference solutions and the equilibrium solution for the case study of carbonate aquifer dissolution by cooling hot water. Temperature (T) solute disequilibrium (Λ) and porosity (θ) in the aquifer are plotted as functions of radial position (r) at different times. The continuous lines represent the Lauwerier solution and the reference solutions (Eqs. 11 and B.1-3 from Appendix B), while the circles in panel (c) denote the equilibrium solution (Eq. 17). (a) The hot flow cools as it flows, the confining rocks heat up, and the thermal front advances downstream. (b) Cooling induces undersaturation (negative disequilibrium, Λ, see Eq. 7). Λ is scaled by the total solubility variation in the system, Δc_s, (refer to the text for the definition of Δc_s). At the inlet, the water is hot and saturated, with $c = c_s(T_{in})$. Undersaturation sharply forms near the inlet ($r \approx 20$ m, as shown in the magnified panel of the region near the inlet) and gradually decreases along the flow path due to dissolution reactions, with Λ approaching zero. As the thermal front advances downstream and the thermal gradients become milder, the Λ curves also flatten. (c) In accordance with the Λ profile, a porosity profile evolves over time. The equilibrium solution closely agrees with the reference solution, except adjacent to the inlet (see magnified panel and text). Quasi-equilibrium conditions are also evident from the small magnitude of Λ, which results from the relatively rapid kinetics (high Da).

The equilibrium model solution matches closely the reference solution and is violated only closely near the inlet ($r < 20$ m; Fig. 2c). The agreement between the solutions and the existence of quasi-

https://doi.org/10.5194/egusphere-2025-733
Preprint. Discussion started: 14 March 2025

equilibrium conditions is supported by the small magnitude of the disequilibrium (Λ) in the reference solution. While the injection of hot, saturated water does not result in porosity changes at the inlet, the equilibrium model, which approximates the reaction rate based on advective and cooling rates (Eq. 14), does not capture this effect. Although the deviation between the solutions is limited to a small region, it may still be significant in the case of dissolution, as locally low porosity and permeability values can impact the overall estimation of aquifer permeability (Roded et al., 2024b). In particular, overestimation of porosity and permeability near the inlet can lead to an overestimation of the aquifer effective permeability. However, in other cases, this deviation may be negligible. Furthermore, in most practical scenarios, the injected fluid is expected to cool slightly as it flows down the well, and therefore, it may already be reactive upon entering the aquifer.

It is noted that the solutions in Section 3.1 and the results shown in Fig. 2 rely on the fundamental assumption of spatial uniformity and symmetry in reactive flow. However, in practical scenarios, dissolution channels (wormholes) may develop at the reaction front (Chadam et al., 1986; Furui et al., 2022; Roded et al., 2021). These wormholes localize reactive flow, creating heterogeneous flow fields that deviate from the assumed symmetry and uniformity. Consequently, the results in Fig. 2 represent only an average solution and do not capture local flow variations accurately.

Additionally, the model was found to apply to the injection of hot, silica-rich water into a sandstone aquifer, where cooling leads to supersaturation, silica precipitation, and porosity reduction, as discussed in Roded et al. (2024b) (not presented). In summary, the results in this section validate the equilibrium solutions against the reference solutions. These results also demonstrate their overall applicability across a broad range of characteristic conditions in natural and applied systems, as further discussed in the Discussion section.

3.2.2. System Shift Over Time

This section analyzes the system state change over time and its evolution toward quasi-equilibrium, as reflected by the differences in predicted reaction rates between the solutions, as functions of time. Conditions of precipitation ($\beta > 0$) are considered with a kinetic rate coefficient nearly four orders of magnitude lower ($\lambda = 5 \cdot 10^{-10}$ m/s), while keeping the rest of the parameters

https://doi.org/10.5194/egusphere-2025-733
Preprint. Discussion started: 14 March 2025

the same as in Section 3.2.1. This scenario corresponds, for example, to calcite precipitation under neutral conditions (Plummer et al., 1978).

Figure 3a presents the results for the reaction rate, Ω, for the reference solution (solid lines, Eqs. B.1 and 3) and the equilibrium solution (dashed lines with circle markers, Eq. 16). The lower reaction rates and reduced Damköhler number, *Da*, result in a larger disequilibrium magnitude, Λ, and greater deviation compared to the case presented in Fig. 2. Additionally, the peak magnitude of disequilibrium is attained further downstream.

Notably, in Fig. 3a, the deviation between the solutions decreases as time progresses. This is also illustrated in Fig. 3b, which shows the error calculated as the difference between the solutions integrated in the radial direction, $Err = (\Omega_{Ref} - \Omega_{Equ})2\pi r dr$, where subscripts Ref and Equ denote reference and equilibrium solutions, respectively. Fig. 3b presents only the positive values of *Err* as the colored regions (the magnitude of the negative values being equal due to solute conservation in the solutions).

The *Err* curves show a progressive decrease and flattening over time. This reduction in *Err* and the closer approach to quasi-equilibrium are attributed to the thermal front advancing downstream. As the thermal front advances and extends, the temperature gradients near the inlet become milder, leading to a decrease in the reaction rate in this region. The temperature gradients also reach further downstream to regions with lower flow velocity and higher local *Da*, causing the deviation between the solutions to diminish. This is illustrated by the black curve, which shows the trend of $1/Da$ with the radial distance from the inlet.

https://doi.org/10.5194/egusphere-2025-733
Preprint. Discussion started: 14 March 2025

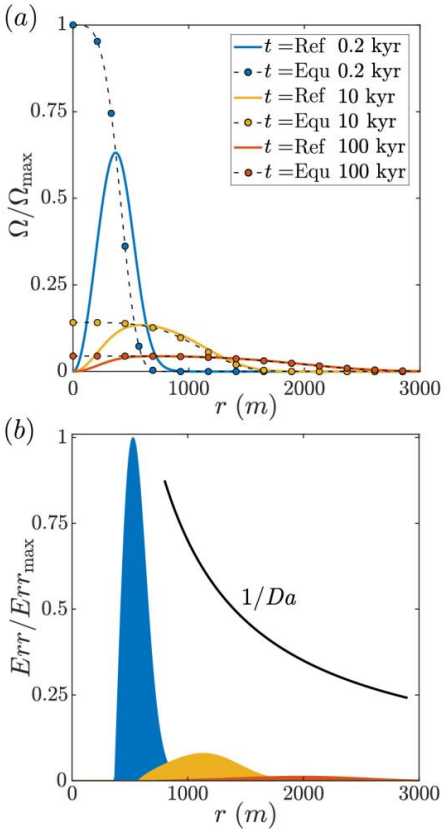

Figure 3. Shift in system state over time and the evolution of distance to equilibrium at low *Da* conditions. (a) Reaction rate, Ω, for the equilibrium solution (Eq. 16) and the reference solution (Eq. B.3) as functions of radial position (*r*) at different times. 'Equ' and 'Ref' in the legend denote the equilibrium and reference solutions, respectively. Notably, the deviation between the solutions decreases as time progresses. (b) This is also illustrated by the plots of the error, *Err*, shown as colored region. *Err* is calculated as the radial integral of the difference between the solutions in (a) (refer to text). The *Err* progressively decreases and flattens over time, reflecting the system approach to quasi-equilibrium as the thermal front advances downstream. As the front stretches, temperature gradients near the inlet become milder and extend into areas with lower flow velocity and higher local *Da*. The trend of 1/*Da* with radial distance from the inlet is shown by the black curve.

3.3. Equilibrium Criterion Derivation

As noted in the Introduction, the applicability of the equilibrium model is determined by the Damköhler number, *Da*, with quasi-equilibrium conditions prevailing when *Da* >1 (Eq. 1). In this section, the factors promoting quasi-equilibrium in the specific settings of the RLP are analyzed,

https://doi.org/10.5194/egusphere-2025-733
Preprint. Discussion started: 14 March 2025

with particular focus on the influence of thermal parameters and time. This analysis enables the derivation of the functional relationship between key parameters, variables, and the system equilibrium state. A key feature of quasi-equilibrium is the close alignment of the thermal and reactive fronts in the aquifer (see cf. Fig. 2a and b). This feature is leveraged to establish a criterion for when these fronts coincide, and equilibrium conditions can be assumed. It is important to note that even when the fronts coincide, far-from-equilibrium conditions may still persist upstream. Nonetheless, the derived functional relationships offer useful guidance.

First, the thermal front end location, r_F, is defined as the position where the temperature deviates slightly from the ambient value, $\varepsilon = (T(r_F)-T_0)/\Delta T$, where $\varepsilon << 1$. Substituting this definition into Eq. 11 leads to

$$\varepsilon = \mathrm{erfc}(a), \quad \text{where} \quad a = \zeta(t) r_F{}^2. \tag{22}$$

For example, for $\varepsilon = 0.01$ $a \approx 1.8$. Then, r_F can be expressed as,

$$r_F = \sqrt{\frac{a}{\zeta(t)}}. \tag{23}$$

Next, an approximate form of the reference solution for disequilibrium is used, assuming quasi-equilibrium and the coalescence of the thermal and reactive fronts (Eq. B.3 in Appendix B; Roded et al., 2024b). In this solution, by substituting the front-end location, r_F, and the condition $\varepsilon \geq \Lambda/\Delta c_s$, we obtain:

$$\varepsilon \geq \frac{\Delta T}{\Delta c_s} \frac{\beta}{\sqrt{\pi}} e^{(-\eta r^2)} \left(\frac{\mathrm{e}^{(\eta r_F^2 - \zeta^2 r_F^4)}}{\frac{\eta}{2\zeta} - \zeta r_F^2} - \frac{2\zeta}{\eta} \right). \tag{24}$$

Substituting the definition from Eq. 23, neglecting early times, and assuming high *Da* and $\eta >> \zeta$, Eq. 24 finally becomes:

$$\varepsilon \geq \frac{\Delta T}{\Delta c_s} \frac{\beta}{\sqrt{\pi}} \frac{2\zeta}{\eta}. \tag{25}$$

https://doi.org/10.5194/egusphere-2025-733
Preprint. Discussion started: 14 March 2025

Noting that $\beta = \Delta c_s/\Delta T$ and explicitly substituting the parameters using Eq. 12 and $\eta = H\pi A_s\lambda/Q$, Eq. 25 becomes,

$$1 \gg \frac{2}{\sqrt{\pi t}}\left(\frac{1}{A_s\lambda}\right)\left(\frac{\sqrt{K_b C_{p_b}}}{HC_{p_f}}\right). \tag{26}$$

Equation 26 defines the conditions under which the thermal and reactive fronts coincide and provides a functional relationship to the state of equilibrium. As shown in the previous section and in Fig. 3, the criterion demonstrates that the system approaches equilibrium as time progresses (with a proportionality of $t^{-1/2}$). The second term in the brackets represents the characteristic timescale of the reaction, $t_R = 1/A_s\lambda$, which, in accordance with the high *Da* condition, indicating that when t_R is small, the system approaches equilibrium more rapidly. The final term in the brackets represents the ratio between thermal parameters, showing that when the confining rock parameters of heat conductivity (K_b) and capacity (C_{pb}) are small, the thermal front advances downstream more quickly, promoting equilibrium. Conversely, when the product HC_{pf} is large, the thermal front also advances quickly downstream, facilitating equilibrium. Notably, the volumetric flow rate (Q) does not appear in the criterion of Eq. 26, as solute advection enhances disequilibrium (in accordance with the *Da* criterion), while thermal advection promotes equilibrium by extending and stretching the thermal front.

This criterion of Eq. 26 can be further rewritten in terms of two functions,

$$1 \gg f(r_F)g(t, r_F), \tag{27}$$

where

$$f(r_F) = \frac{lu(r_F)}{A_s\lambda} \quad \text{and} \quad g(t, r_F) = \frac{2}{\sqrt{\pi t}}\frac{\sqrt{K_b C_{p_b}}}{lu(r_F)HC_{p_f}}. \tag{28}$$

The first function, $f(r_F)$ can be referred to as a dynamic *Da* number that changes with the position of r_F and describes the relative effect of advective transport versus reaction. The second function $g(t,r_F)$ accounts for the evolution of the thermal front with time.

https://doi.org/10.5194/egusphere-2025-733
Preprint. Discussion started: 14 March 2025

3.4. Development of Coalesced Fronts

Equation 23, along with one that applies to the planar case, can be used to infer the coalesced thermal and reactive front extensions, $\underline{x_F}$ and r_F, under quasi-equilibrium conditions. These provide:

$$x_F(t) = \frac{aHC_{p_f}u}{\sqrt{K_b C_{p_b}}} t^{\frac{1}{2}}, \quad \text{and} \quad r_F(t) = \sqrt{\frac{aQC_{p_f}}{\pi\sqrt{K_b C_{p_b}}}} t^{\frac{1}{4}}. \tag{29}$$

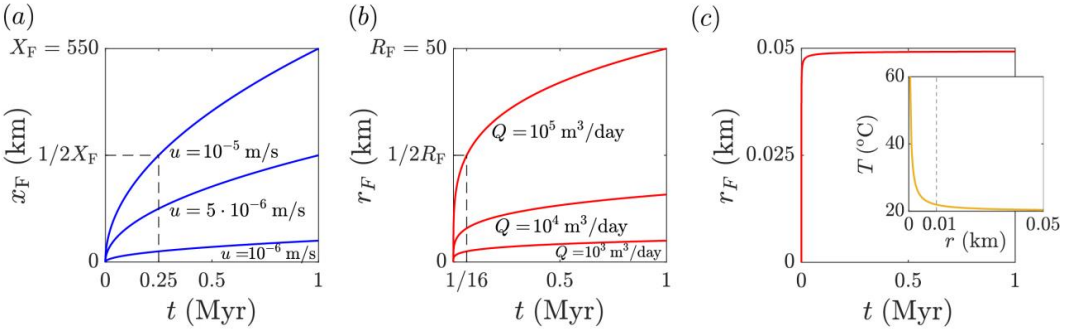

Figure 4. Elongation of the coalesced thermal and reactive fronts, x_F and r_F, over time for different velocities, u, and flow rates, Q, respectively (a, b), and the low-flow-rate limit assuming conduction only (c). (a, b) The fronts elongation over time is proportional to $t^{1/2}$ and $t^{1/4}$, respectively, (Eq. 29), and hence the rate of elongation decreases substantially faster for the radial case and at lower flow rates. To illustrate this, half of the final calculated extension, $1/2X_F$ is marked and shown to be reached in 1/4 of the time, while in the radial case, $1/2R_F$ is approached after 1/16 of the time (see dashed lines). (c) The low-flow-rate limit is shown using the quasi-steady-state solution for conduction from a point source in an infinite space. The inner inset and the orange curve display the temperature profile, with the dashed line showing that almost complete cooling occurs within 10 m. In this case, the front becomes quasi-stationary on a timescale of tens of years. This scenario is particularly relevant under natural conditions, demonstrating that the reactive front may become essentially stationary (see the Discussion section). Parameter values used are as in Section 3.2.1 and Appendix C, and flow rate and velocity values are indicated in the figure.

For demonstration, panels a-b of Fig. 4 show x_F and r_F plotted for three different velocities, u, and flow rates, Q. This illustrates the advancement rate of the front decays substantially faster for the radial case (the decay and the derivative of r_F is proportional to $t^{-3/4}$, compared to the planar case, where it follows $t^{-1/2}$). Additionally, in Fig. 4c is shown r_F for conduction only from a point source

https://doi.org/10.5194/egusphere-2025-733
Preprint. Discussion started: 14 March 2025

in an infinite space, demonstrating the low-flow-rate limit. The inset presents a quasi-steady-state solution of the temperature profile (Stauffer et al., 2014). This scenario is particularly relevant to natural conditions which are often associated with low flow rates (Garven, 1995; Klimchouk et al., 2017).

In this case, the front can becomes quasi-stationary on a timescale of tens of years (Roded et al., 2023) and the reactive front can become nearly stationary, as will be further discussed in the Discussion section below. Lastly, it is recalled that while the solutions assume an infinite caprock thickness, if the thermal front reaches the surface, a greater heat exchange between the aquifer and the caprock is expected, which would reduce the thermal front advancement rate and extension.

4. Discussion

4.1. Case Studies and Applicability of the Equilibrium Model

Figure 5 presents a phase diagram distinguishing between conditions where the equilibrium model is applicable and those far from equilibrium. The diagram is based on the Damköhler number ($Da = t_A/t_R = l\lambda A_s/u$) and Eq. 1, with the diagonal line marking the transition at $Da > 1$ (Da_{cr}). Hotter colors denote higher Da values and conditions closer to equilibrium. As reactivity ($1/t_R$) increases, the equilibrium model becomes applicable over a wider range of flow velocities, u, or smaller characteristic length scales, l, represented as $1/t_A = u/l$. Here, l represents the local characteristic length scale of thermal and solubility variations (see Appendix A).

The diagram also positions key fluid-rock interaction processes according to their characteristic reactivity. At the top are common carbonates, i.e., limestone and dolomite, which typically exhibit high reaction rates and are highly prone to alteration (with λ typically ranging from 10^{-8} to 10^{-4} m/s; Dreybrodt et al., 2005; Peng et al., 2015; Plummer et al., 1978). Silica precipitation is also prevalent in hydrothermal settings (Glassley, 2014; Huenges and Ledru, 2011; Sibson et al., 1975) and is characterized by relatively high reactivity, with a typical rate constant of $\lambda = 5^{\bullet}\ 10^{-10}$ m/s (Rimstidt and Barnes, 1980). In contrast, while non-crystalline silica (amorphous) precipitates relatively quickly, quartz dissolution is typically slower by several orders of magnitude (Rimstidt and Barnes, 1980).

https://doi.org/10.5194/egusphere-2025-733
Preprint. Discussion started: 14 March 2025

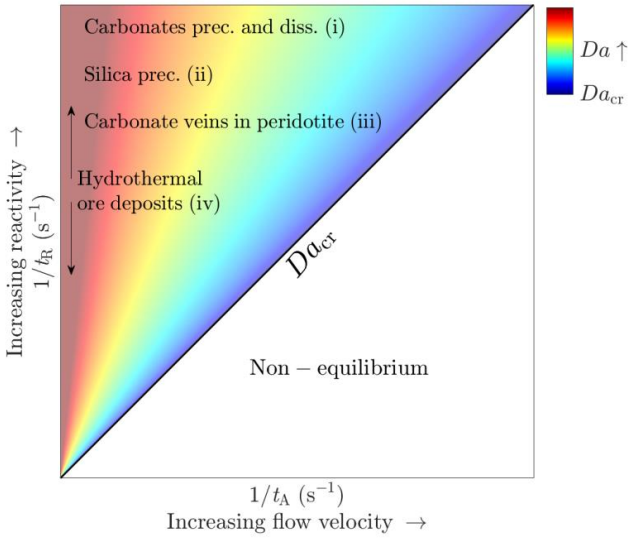

Figure 5. A diagram illustrating the applicability of the equilibrium model and highlighting important fluid-rock interaction processes. The Damköhler number is used to differentiate between far-from-equilibrium conditions and quasi-equilibrium, where the equilibrium model can be assumed when $Da > Da_{cr}$, with Da_{cr} defined as a threshold where $Da_{cr} > 1$. Da_{cr} is represented by the diagonal black line on the diagram, with hot colors indicating high Da values and proximity to equilibrium. The diagram is based on Eq. 1 and plots $1/t_R$ versus $1/t_A$ (where $1/t_R = \lambda A_s$ and $1/t_A = u/l$). Main fluid-rock interaction processes are indicated on the diagram according to their typical reactivity: (i) carbonate dissolution or precipitation, (ii) silica precipitation, (iii) carbonate vein formation in peridotites, and (iv) hydrothermal ore deposits. In higher reactivity systems, the equilibrium model is applicable under higher flow velocities, and/or small l and relatively large thermal variations, i.e., shorter t_A.

The position of these processes on the diagram, as also demonstrated in Section 3.2.1, indicates the applicability of the equilibrium model even at relatively high flow rates. This is especially significant, as high flow rates are characteristic of applications such as groundwater storage and recovery, aquifer thermal storage, and geothermal reinjection (Diaz et al., 2016; Fleuchaus et al., 2018; Maliva, 2019). It is noted that the range of reactivity typically spans several orders of magnitude and is associated with kinetics and large variability in reactive surface area, especially between fractured and porous media (Deng and Spycher, 2019; Maher et al., 2006; Pacheco and Alencoão, 2006; Seigneur et al., 2019).

https://doi.org/10.5194/egusphere-2025-733
Preprint. Discussion started: 14 March 2025

Additional important settings in which thermally driven reactions may play a significant role include the formation of carbonate veins in peridotites by ascending CO_2-rich hydrothermal flow (Kelemen et al., 2011; Menzel et al., 2024). The CO_2-rich fluids first dissolve the rock minerals, primarily olivine. Then, as the pH rises and cation enrichment occurs, carbonate precipitation, primarily magnesite, takes place further along the upward flow path. Commonly, the rate-limiting step in the mineral carbonation process is the slower kinetics of dissolution (Kelemen et al., 2019; Kelemen et al., 2011). The solubility of olivine is retrograde, as evidenced by the exothermic nature of the reaction (Kaszuba et al., 2013; Prigiobbe et al., 2009). Under these conditions, the ascending flow along a decreasing geothermal gradient is expected to promote undersaturation, enhance the dissolution reaction (Kelemen et al., 2013), and facilitate the development of an extended reactive front. Considering the typically low rates of ascending hydrothermal flow (e.g., $u < 10^{-7}$ m/s; Garven, 1995), along with the relatively rapid olivine dissolution kinetics and high rate constant (Rimstidt, 2015; Rimstidt et al., 2012), it suggests that *Da* is large. Consequently, mineral carbonation and vein formation occur under quasi-equilibrium conditions, making the equilibrium model applicable.

Lastly, a prominent application in which thermally driven reactions play a major role is the hydrothermal formation of ore deposits. These processes involve a wide range of reactions and genetic origins of hydrothermal fluids. Such fluids include metamorphic and meteoric-origin waters, which evolve through different fluid-fluid or fluid-rock interactions, as well as fluids originating directly from magmatic intrusions (so-called magmatic-hydrothermal fluids; Ingebritsen and Appold, 2012; Robb, 2005). A particularly intriguing phenomenon, often primarily controlled by the dependence of solubility on temperature, is the zoning of metals and minerals, which is commonly observed at various field scales. In these cases, regular belts of different precipitants form progressively as the distance from the hydrothermal fluid source increases. This pattern is often largely influenced by the solubility of the minerals and their precipitation as a result of cooling along the flow path (Kouzmanov and Pokrovski, 2012; Robb, 2005).

4.2. Evolution of Field-scale Reactive Fronts

The dominance of the thermal front over the reactive front and their coalescence under quasi-equilibrium conditions allowed for the exploration of the reactive front evolution under different

https://doi.org/10.5194/egusphere-2025-733
Preprint. Discussion started: 14 March 2025

settings, as discussed in Section 3.4. Specifically, the analysis demonstrates that in radial or spherical settings (i.e., flows spreading from a point source) at relatively low flow rates (e.g., several cubic meters per day), a quasi-steady state is achieved over timescales on the order of tens to hundreds of years. Such a cooling process can also induce very steep geothermal gradients. These gradients may be two orders of magnitude larger than the typical basal geothermal gradient formed by Earth heat flow (e.g., 0.025 °C/m ;Davies, 2013), as shown in the temperature profile in the inset of Fig. 4c (see also Roded et al. (2023).

A prominent example of such conditions is porphyry-type deposits. In these systems, magmatic-hydrothermal fluids are expelled from a crystallizing magmatic intrusion. These fluids then spread away (typically upward and laterally) from the source while cooling and precipitating various metals and minerals (Ingebritsen & Appold, 2012; Robb, 2005). The results here suggest that reactive mineral deposition fronts associated with porphyry ore deposits are essentially stationary for a large part of their lifetime, typically ranging from tens of thousands to millions of years (Cooke et al., 2014; Robb, 2005). The results presented here also contrast with the view that thermal gradients are too weak to promote precipitation (Cooke et al., 2014). Another example involves hypogenic karst and cave formation driven by upwelling hydrothermal flow, which discharges through a permeable fault pathway, spreads radially in a confined aquifer, and cools (Roded et al., 2023, 2024a). In this case, the results suggest that the alteration front or the cave system may exhibit quasi-constant and final dimensions.

However, in the planar case of uniformly ascending hydrothermal flow and mineral carbonation in veins, steady-state thermal conditions are presumably reached quickly. This occurs compared to the timescale of vein evolution, which spans tens of thousands of years or longer (Früh-Green et al., 2003). Similarly, in any case of hydrothermal ore deposit formation by ascending flow (i.e., hypogene), steady-state thermal conditions may be reached quickly. In both scenarios, the hot ascending flow alters the background geothermal gradient and may achieve steady-state over relatively short timescales (Ingebritsen et al., 2010; Roded et al., 2013).

In these cases, the timescale for the thermal front to reach a steady-state suggests that if reactive processes span periods comparable to the geological timescale of tectonic processes, spatial alterations will depend on these slower tectonic timescales. These tectonic timescales are

https://doi.org/10.5194/egusphere-2025-733
Preprint. Discussion started: 14 March 2025

associated with processes such isostasy due to erosion, subduction, or orogenic activity. A well-known example is the alteration of the geothermal gradient caused by surface erosion or sediment deposition (Haenel et al., 2012; Turcotte and Schubert, 2002). In response to tectonic changes, the slowly varying subsurface thermal distribution drives the gradual migration of the reactive front.

4 Summary and Conclusions

In this work, the equilibrium assumption is used to derive thermally driven reactive transport solutions for the RLP (reactive Lauwerier problem) in both Cartesian and radial coordinates. The solution for porosity evolution is then validated against a reference solution and a case study of CO_2-rich hot water injection from a single well into a carbonate aquifer, leading to cooling and calcite dissolution. The limitations of the solution are analyzed as a function of time and the progression of the thermal front. Under these radial settings, as the front advances downstream into regions with lower flow velocity and higher *Da*, and the error associated with the equilibrium assumption diminishes. This finding motivates the derivation of a specific criterion and functional relationship to guide quasi-equilibrium conditions in the RLP, incorporating time and thermal parameters. Specifically, this criterion is expressed through two functions: a dynamic *Da* number and a thermal parameter function that accounts for front elongation.

Next, the unique feature of the thermal front controlling the reactive front and their coalescence under quasi-equilibrium conditions is used to explore their evolution over time. This is examined in both planar and radial settings, as well as a function of flow rate. The growth rate in the radial case decreases much more rapidly, and it is shown that, in the low-flow-rate limit, the front can become stationary in a relatively short period. The applicability of the equilibrium model for important fluid-rock interaction processes is then discussed and positioned on a diagram based on the Damköhler number, demonstrating the applicability of the equilibrium assumption under different conditions. The processes examined include sedimentary reservoir evolution, mineral carbonation in peridotite, and ore deposit formation by hydrothermal flows. Finally, it is emphasized that thermally driven reactive fronts near equilibrium often cease to expand after the early stages. Instead, they remain stationary, with their evolution governed by geological processes. These processes, such as tectonics or surface erosion and deposition, occur on much longer timescales.

https://doi.org/10.5194/egusphere-2025-733
Preprint. Discussion started: 14 March 2025

Appendix A: *Da* Condition for Applicability of the Equilibrium Model

Assuming quasi-equilibrium conditions and equating the reaction rates given in Eqs. 6 and 14 yields,

$$u\frac{\partial c_s(T)}{\partial r} \approx A_s\lambda\big(c - c_s(T)\big). \tag{A.1}$$

Assuming on a local scale that

$$\frac{\partial c_s}{\partial r} \approx \frac{\Delta c_{s\varepsilon}}{l}, \tag{A.2}$$

where, l represents a characteristic length scale over which temperature and solubility change, with the magnitude of $\Delta c_{s\varepsilon}$ is $\varepsilon\Delta c_s$, where $\varepsilon << 1$ (e.g., $\varepsilon = 0.01$) and Δc_s denotes the absolute solubility change in the system ($\Delta c_s = |c_s(T_{in}) - c_s(T_0)|$). Assuming quasi-equilibrium conditions and that $\Delta c_{s\varepsilon}/(c - c_s(T)) > 1$, Eq. A.1 can be rearranged to give,

$$Da = \frac{lA_s\lambda}{u_A} > 1, \tag{A.3}$$

where Da is the Damköhler number, and the velocity u is replaced by the characteristic fluid velocity u_A in the above equation.

Appendix B: Radial RLP Solutions

The RLP solution for the solute disequilibrium is given by,

$$\Lambda = \Delta T\beta e^{\left(\frac{\eta^2}{4\zeta^2} - \eta r^2\right)}\left(\mathrm{erf}\left[\zeta r^2 - \frac{\eta}{2\zeta}\right] + \mathrm{erf}\left[\frac{\eta}{2\zeta}\right]\right). \tag{B.1}$$

A closed-form expression for the temporal and spatial evolution of porosity, θ, is given by,

$$\theta(r,t) = \theta_0 + 4\frac{\zeta^2 t}{\eta^2}\frac{\lambda A_s\Delta T\beta}{\nu c_{sol}}\left(-e^{\eta/4\left(\frac{\eta}{\zeta^2} - 4r^2\right)}\left(\mathrm{erf}\left[\zeta r^2 - \frac{\eta}{2\zeta}\right] + \mathrm{erf}\left[\frac{\eta}{2\zeta}\right]\right) + \frac{\eta}{\zeta\sqrt{\pi}}e^{-\eta r^2}\right.$$
$$\left. + \mathrm{erf}[\zeta r^2](1 - \eta r^2) - \frac{\eta}{\zeta\sqrt{\pi}}e^{-\zeta^2 r^4} + \eta r^2 - 1\right). \tag{B.2}$$

https://doi.org/10.5194/egusphere-2025-733
Preprint. Discussion started: 14 March 2025

For efficient computation and preventing integer overflow (Press et al., 2007), an approximate solution of Eq. B.1 is developed using the first-order asymptotic expansion of erfc,

$$\Lambda = \frac{\Delta T \beta}{\sqrt{\pi}} e^{(-\eta r^2)} \left(\frac{e^{(\eta r^2 - \zeta^2 r^4)}}{\frac{\eta}{2\zeta} - \zeta r^2} - \frac{2\zeta}{\eta} \right). \quad (B.3)$$

To prevent integer overflow errors, Eq. B.3 is used to calculate the undersaturation and reaction rate profiles in Figs. 2b and 3a, respectively. It is also used to iteratively solve numerically to obtain the porosity profile at later times, as shown in Fig. 3c (t = 100 kyr). The accuracy of the approximation in Eq. B.3 was validated by comparing it with the full solution in Eq. C.1, which is solvable for early times ($t \approx 1$ yr). Additionally, the accuracy of Eq. C.3 and the iterative solutions was also validated by solving for the porosity profile and comparing the results to those obtained using the full solution in Eq. B.2 for t = 10 kyr (Roded et al., 2024b).

Appendix C: Parameter Values

Table 1. Parameter values used in the simulation in Section 3.2.1.

Aquifer thickness	H = 4 m
Initial porosity	θ_0 = 0.05
Total volumetric flow rate[1]	Q = 500 m^3/s
Initial aquifer temperature[2]	T_0 = 20 °C
Injection temperature[2]	T_{in} = 60 °C
Fluid volumetric heat capacity[2]	C_{pf} = 4.2·10^6 J m^{-3} °C^{-1}
Rock volumetric heat capacity[2]	C_{pb} = 3.12·10^6 J/(m^3 °C)
Rock thermal conductivity[2]	K_b = 3 W m^{-1} °C^{-1}
Calcite rate coefficient[3]	λ = 10^{-6} m/s
Fractured carbonates specific reactive surface area[5]	A_s = 10 m^{-1}
Calcite mineral concentration[3]	c_{sol} = 2.7·10^4 mol/m^3
Solubility change parameter calcite[7]	β = -0.075 mol m^{-3} °C^{-1}
Stoichiometry coefficient[3,4]	ν = 1

1-Glassley (2014); 2-Huenges and Ledru (2011); 3-Palmer (1991); 4-Rimstidt and Barnes (1980); 5- see text; 6-Hussaini and Dvorkin (2021) and Lai et al. (2015); 7-Roded et al. (2023).

https://doi.org/10.5194/egusphere-2025-733
Preprint. Discussion started: 14 March 2025

Appendix D: Nomenclature

Roman			
a	Error function argument,	t_R	Characteristic timescale of reaction, s
A_s	Specific reactive surface area, m^2/m^3	T	Temperature, °C
c	Solute concentration, mol/m^3	u	Fluid velocity, m/s
c_s	Saturation concentration, mol/m^3	u_A	Characteristic fluid velocity, m/s
c_{sol}	Concentration of soluble solid, mol/m^3	x	Coordinate, m
Cp	Volumetric heat capacity, $J/(m^3\,°C)$	y	Coordinate, m
Da	Damköhler number	z	Coordinate, m
Da_{cr}	Critical Damköhler number		**Greek**
D_s	Solute dispersivity, m^2/s	α	Thermal diffusivity, m^2/s
D_T	Thermal dispersivity, m^2/s	β	Solubility change parameter, $mol/(m^3\,°C)$
erf	Error function	Δ	Total difference
erfc	Complementary error function	$\Delta c_{s\varepsilon}$	Local change in solubility
Err	Error	ε	Number much smaller than one
f	Equilibrium criterion function	η	Parameter group, m^{-2}
g	Equilibrium criterion function	θ	Porosity
H	Aquifer thickness, m	$\boldsymbol{\Theta}$	Heat exchange term, W/m^2
K	Thermal conductivity, $W\,m^{-1}\,°C^{-1}$	λ	Reaction rate coefficient, m/s
l	Local characteristic length scale, m	Λ	Solute disequilibrium, mol/m^3
l_C	Characteristic length scale of conduction, m	Γ	Gamma function
$\boldsymbol{n}$	Unit vector, m	μ	Fluid viscosity, Pa s
p	Fluid pressure, Pa	ν	Stoichiometric coefficient
Pe_s	Solute Péclet number	ζ	Parameter group, m^{-2}
Pe_T	Thermal Péclet number	ξ	Lateral coordinate, $\xi = r$ or x, m
Q	Total volumetric flow rate, m^3/s	ω	Parameter group, m^{-1}
r	Coordinate, m	Ω	Reaction rate, $mol\,m^{-3}\,s^{-1}$
r_F	Front end location, radial case, m		**Subscripts**
R_F	Final front end location, radial case, m	b	Bulk rock
x_F	Front end location, planar case, m	Equ	Equilibrium solution
X_F	Final front end location, planar case, m	f	Fluid
t	Time, s	in	Inlet
t'	Time parameter, s	max	Max
t_A	Characteristic timescale of advection, s	Ref	Reference solution
t_C	Characteristic timescale of conduction, s	0	Initial average quantity

https://doi.org/10.5194/egusphere-2025-733
Preprint. Discussion started: 14 March 2025

Code & Data availability:

The MATLAB codes and data generated in this study are available to reviewers and upon request from the author.

Competing interests:

The author declares no competing interests.

Acknowledgments:

The research was supported as part of the Center on Geo-processes in Mineral Carbon Storage, an Energy Frontier Research Center funded by the U.S. Department of Energy (DOE), Office of Science, Basic Energy Sciences (BES), under Award # DE-SC0023429.

References

Anderson, R.: Infectious diseases of humans: dynamics and control, Oxford University Press, 1991.

Andre, B. J. and Rajaram, H.: Dissolution of limestone fractures by cooling waters: Early development of hypogene karst systems, Water Resour. Res., 41, 2005.

Appelo, C. A. J. and Postma, D.: Geochemistry, groundwater and pollution, CRC press, 2004.

Bekri, S., Thovert, J. F., and Adler, P. M.: Dissolution of porous media, Chem Eng Sci, 50, 2765–2791, 1995.

Chadam, J., Hoff, D., Merino, E., Ortoleva, P., and Sen, A.: Reactive infiltration instabilities, IMA J. Appl. Math., 36, 207–221, 1986.

Chaudhuri, A., Rajaram, H., and Viswanathan, H.: Early-stage hypogene karstification in a mountain hydrologic system: A coupled thermohydrochemical model incorporating buoyant convection, Water Resour. Res., 49, 5880–5899, 2013.

Chen, C. and Reddell, D. L.: Temperature distribution around a well during thermal injection and a graphical technique for evaluating aquifer thermal properties, Water Resour. Res., 19, 351–363, 1983.

Cooke, D., Hollings, P., Wilkinson, J., Tosdal, R., and Turekian, H.: 13.14—Geochemistry of porphyry deposits, Treatise Geochem., 13, 357–381, 2014.

Cornish-Bowden, A.: Fundamentals of enzyme kinetics, John Wiley & Sons, 2013.

Corson, L. T. and Pritchard, D.: Thermosolutal convection in an evolving soluble porous medium, J. Fluid Mech., 832, 666–696, 2017.

Coudrain-Ribstein, A., Gouze, P., and de Marsily, G.: Temperature-carbon dioxide partial pressure trends in confined aquifers, Chem. Geol., 145, 73–89, 1998.

Craw, D.: Fluid flow at fault intersections in an active oblique collision zone, Southern Alps, New Zealand, J. Geochem. Explor., 69, 523–526, 2000.

Davies, J. H.: Global map of solid Earth surface heat flow, Geochem. Geophys. Geosystems, 14, 4608–4622, 2013.

https://doi.org/10.5194/egusphere-2025-733
Preprint. Discussion started: 14 March 2025

Deng, H. and Spycher, N.: Modeling reactive transport processes in fractures, Rev. Mineral. Geochem., 85, 49–74, 2019.

Deng, H., Molins, S., Steefel, C., DePaolo, D., Voltolini, M., Yang, L., and Ajo-Franklin, J.: A 2.5 D reactive transport model for fracture alteration simulation, Environ. Sci. Technol., 50, 7564–7571, 2016.

Diaz, A. R., Kaya, E., and Zarrouk, S. J.: Reinjection in geothermal fields− A worldwide review update, Renew. Sustain. Energy Rev., 53, 105–162, 2016.

Dreybrodt, W., Gabrovšek, F., and Romanov, D.: Processes of Speleogenesis: A Modeling Approach, Založba ZRC, 2005.

Fleuchaus, P., Godschalk, B., Stober, I., and Blum, P.: Worldwide application of aquifer thermal energy storage–A review, Renew. Sustain. Energy Rev., 94, 861–876, 2018.

Früh-Green, G. L., Kelley, D. S., Bernasconi, S. M., Karson, J. A., Ludwig, K. A., Butterfield, D. A., Boschi, C., and Proskurowski, G.: 30,000 years of hydrothermal activity at the Lost City vent field, Science, 301, 495–498, 2003.

Furui, K., Abe, T., Watanabe, T., and Yoshioka, K.: Phase-field modeling of wormhole formation and growth in carbonate matrix acidizing, J. Pet. Sci. Eng., 209, 109866, 2022.

Garven, G.: Continental-scale groundwater flow and geologic processes, Annu. Rev. Earth Planet. Sci., 23, 89–117, 1995.

Glassley, W. E.: Geothermal energy: renewable energy and the environment, CRC press, 2014.

Haenel, R., Stegena, L., and Rybach, L.: Handbook of terrestrial heat-flow density determination: with guidelines and recommendations of the International Heat Flow Commission, Springer Science & Business Media, 2012.

Hidalgo, J. J., Fe, J., Cueto-Felgueroso, L., and Juanes, R.: Scaling of convective mixing in porous media, Phys. Rev. Lett., 109, 264503, 2012.

Huenges, E. and Ledru, P.: Geothermal energy systems: exploration, development, and utilization, John Wiley & Sons, 2011.

Hussaini, S. R. and Dvorkin, J.: Specific surface area versus porosity from digital images, J. Pet. Sci. Eng., 196, 107773, 2021.

Ingebritsen, S., Geiger, S., Hurwitz, S., and Driesner, T.: Numerical simulation of magmatic hydrothermal systems, Rev. Geophys., 48, 2010.

Ingebritsen, S. E. and Appold, M.: The physical hydrogeology of ore deposits, Econ. Geol., 107, 559–584, 2012.

Jamtveit, B. and Yardley, B.: Fluid flow and transport in rocks: mechanisms and effects, Springer Science & Business Media, 1996.

Kaszuba, J., Yardley, B., and Andreani, M.: Experimental perspectives of mineral dissolution and precipitation due to carbon dioxide-water-rock interactions, Rev. Mineral. Geochem., 77, 153–188, 2013.

Kelemen, P., Park, A., Matter, J., Gadikota, G., Lisabeth, H., and Zhu, W.: Geo-Chemo-Mechanical Studies for Permanent CO {sub 2} Storage in Geologic Reservoirs, Columbia Univ., New York, NY (United States), 2013.

Kelemen, P., Benson, S. M., Pilorgé, H., Psarras, P., and Wilcox, J.: An overview of the status and challenges of CO2 storage in minerals and geological formations, Front. Clim., 1, 9, 2019.

https://doi.org/10.5194/egusphere-2025-733
Preprint. Discussion started: 14 March 2025

Kelemen, P. B., Matter, J., Streit, E. E., Rudge, J. F., Curry, W. B., and Blusztajn, J.: Rates and mechanisms of mineral carbonation in peridotite: natural processes and recipes for enhanced, in situ CO2 capture and storage, Annu. Rev. Earth Planet. Sci., 39, 545–576, 2011.

Klimchouk, A., Palmer, A. N., De Waele, J., Auler, A. S., and Audra, P.: Hypogene karst regions and caves of the world, Springer, 2017.

Kolditz, O., Shao, H., Wang, W., and Bauer, S.: Thermo-Hydro-Mechanical Chemical Processes in Fractured Porous Media: Modelling and Benchmarking, Springer, 2016.

Kouzmanov, K. and Pokrovski, G. S.: Hydrothermal controls on metal distribution in porphyry Cu (-Mo-Au) systems, 2012.

Ladd, A. J. C. and Szymczak, P.: Use and misuse of large-density asymptotics in the reaction-infiltration instability, Water Resour. Res., 53, 2419–2430, 2017.

Lai, P., Moulton, K., and Krevor, S.: Pore-scale heterogeneity in the mineral distribution and reactive surface area of porous rocks, Chem. Geol., 411, 260–273, 2015.

Lauwerier, H.: The transport of heat in an oil layer caused by the injection of hot fluid, Appl. Sci. Res. Sect. A, 5, 145–150, 1955.

Lichtner, P. C.: The Quasi-Stationary State Approximation to Fluid/Rock Reaction: Local Equilibrium Revisited, in: Diffusion, Atomic Ordering, and Mass Transport: Selected Topics in Geochemistry, edited by: Ganguly, J., Springer US, New York, NY, 452–560, 1991.

Lichtner, P. C., Steefel, C. I., and Oelkers, E. H.: Reactive transport in porous media, Walter de Gruyter GmbH & Co KG, 1996.

Lighthill, M. J. and Whitham, G. B.: On kinematic waves II. A theory of traffic flow on long crowded roads, Proc. R. Soc. Lond. Ser. Math. Phys. Sci., 229, 317–345, 1955.

MacQuarrie, K. T. and Mayer, K. U.: Reactive transport modeling in fractured rock: A state-of-the-science review, Earth-Sci. Rev., 72, 189–227, 2005.

Maher, K., Steefel, C. I., DePaolo, D. J., and Viani, B. E.: The mineral dissolution rate conundrum: Insights from reactive transport modeling of U isotopes and pore fluid chemistry in marine sediments, Geochim. Cosmochim. Acta, 70, 337–363, 2006.

Maliva, R. G.: Anthropogenic aquifer recharge: WSP methods in water resources evaluation series no. 5, Springer, 2019.

Menzel, M. D., Sieber, M. J., and Godard, M.: From peridotite to listvenite–perspectives on the processes, mechanisms and settings of ultramafic mineral carbonation to quartz-magnesite rocks, Earth-Sci. Rev., 104828, 2024.

Micklethwaite, S. and Cox, S. F.: Progressive fault triggering and fluid flow in aftershock domains: Examples from mineralized Archaean fault systems, Earth Planet. Sci. Lett., 250, 318–330, 2006.

Molins, S. and Knabner, P.: Multiscale approaches in reactive transport modeling, Rev. Mineral. Geochem., 85, 27–48, 2019.

Mullins, W. W. and Sekerka, R. F.: Morphological stability of a particle growing by diffusion or heat flow, J. Appl. Phys., 34, 323–329, 1963.

https://doi.org/10.5194/egusphere-2025-733
Preprint. Discussion started: 14 March 2025

Pacheco, F. A. L. and Alencoão, A. M. P.: Role of fractures in weathering of solid rocks: narrowing the gap between laboratory and field weathering rates, J. Hydrol., 316, 248–265, 2006.

Palmer, A. N.: Origin and morphology of limestone caves, Geol. Soc. Am. Bull., 103, 1–21, 1991.

Pandey, S., Vishal, V., and Chaudhuri, A.: Geothermal reservoir modeling in a coupled thermo-hydro-mechanical-chemical approach: a review, Earth-Sci. Rev., 185, 1157–1169, 2018.

Peng, C., Crawshaw, J. P., Maitland, G. C., and Trusler, J. P. M.: Kinetics of calcite dissolution in CO2-saturated water at temperatures between (323 and 373) K and pressures up to 13.8 MPa, Chem Geol, 403, 74–85, 2015.

Phillips, O. M.: Geological fluid dynamics: sub-surface flow and reactions, Cambridge University Press, 2009.

Plummer, L. N., Wigley, T. M. L., and Parkhurst, D. L.: The kinetics of calcite dissolution in CO2-water systems at 5 degrees to 60 degrees C and 0.0 to 1.0 atm CO2, Am. J. Sci., 278, 179–216, https://doi.org/10.2475/ajs.278.2.179, 1978.

Press, W. H., Teukolsky, S. A., Vetterling, W. T., and Flannery, B. P.: Numerical recipes: The art of scientific computing, Cambridge university press, 2007.

Prigiobbe, V., Hänchen, M., Costa, G., Baciocchi, R., and Mazzotti, M.: Analysis of the effect of temperature, pH, CO2 pressure and salinity on the olivine dissolution kinetics, Energy Procedia, 1, 4881–4884, 2009.

Rawal, C. and Ghassemi, A.: A reactive thermo-poroelastic analysis of water injection into an enhanced geothermal reservoir, Geothermics, 50, 10–23, 2014.

Rimstidt, J. D.: Diffusion control of quartz and forsterite dissolution rates, Appl. Geochem., 61, 99–108, 2015.

Rimstidt, J. D. and Barnes, H.: The kinetics of silica-water reactions, Geochim. Cosmochim. Acta, 44, 1683–1699, 1980.

Rimstidt, J. D., Brantley, S. L., and Olsen, A. A.: Systematic review of forsterite dissolution rate data, Geochim. Cosmochim. Acta, 99, 159–178, 2012.

Robb, L.: Introduction to ore-forming processes, John Wiley & Sons, 2005.

Roded, R. and Dalton, L. E.: Stability of two-phase flow with interfacial flux in porous media: CO2 mineralization, Phys. Fluids, 36, 2024.

Roded, R., Shalev, E., and Katoshevski, D.: Basal heat-flow and hydrothermal regime at the Golan-Ajloun hydrological basins, J. Hydrol., 476, 200–211, 2013.

Roded, R., Aharonov, E., Holtzman, R., and Szymczak, P.: Reactive flow and homogenization in anisotropic media, Water Resour. Res., p.e2020WR027518., 2020.

Roded, R., Szymczak, P., and Holtzman, R.: Wormholing in anisotropic media: Pore-scale effect on large-scale patterns, Geophys. Res. Lett., e2021GL093659, 2021.

Roded, R., Aharonov, E., Frumkin, A., Weber, N., Lazar, B., and Szymczak, P.: Cooling of hydrothermal fluids rich in carbon dioxide can create large karst cave systems in carbonate rocks, Commun. Earth Environ., 4, 465, https://doi.org/10.1038/s43247-023-01082-z, 2023.

Roded, R., Langford, B., Aharonov, E., Szymczak, P., Ullman, M., Yaaran, S., Lazar, B., and Frumkin, A.: Hypogene speleogenesis in carbonates by cooling hydrothermal flow: The case of Mt. Berenike caves, Israel, Int. J. Speleol., 53, 8, 2024a.

https://doi.org/10.5194/egusphere-2025-733
Preprint. Discussion started: 14 March 2025

Roded, R., Aharonov, E., Szymczak, P., Veveakis, M., Lazar, B., and Dalton, L. E.: Solutions and case studies for thermally driven reactive transport and porosity evolution in geothermal systems (reactive Lauwerier problem), Hydrol. Earth Syst. Sci., 28, 4559–4576, 2024b.

Seigneur, N., Mayer, K. U., and Steefel, C. I.: Reactive transport in evolving porous media, Rev. Mineral. Geochem., 85, 197–238, 2019.

Sibson, R., Moore, J. M. M., and Rankin, A.: Seismic pumping—a hydrothermal fluid transport mechanism, J. Geol. Soc., 131, 653–659, 1975.

Solow, R. M.: A contribution to the theory of economic growth, Q. J. Econ., 70, 65–94, 1956.

Stauffer, F., Bayer, P., Blum, P., Molina-Giraldo, N., and Kinzelbach, W.: Thermal use of shallow groundwater, 2014.

Steefel, C. I. and Maher, K.: Fluid-Rock Interaction: A Reactive Transport Approach, Rev. Mineral. Geochem., 70, 485–532, https://doi.org/10.2138/rmg.2009.70.11, 2009.

Szymczak, P. and Ladd, A. J. C.: Reactive-infiltration instabilities in rocks. Fracture dissolution, J. Fluid Mech., 702, 239–264, 2012.

Taron, J. and Elsworth, D.: Thermal–hydrologic–mechanical–chemical processes in the evolution of engineered geothermal reservoirs, Int. J. Rock Mech. Min. Sci., 46, 855–864, 2009.

Tripp, G. I. and Vearncombe, J. R.: Fault/fracture density and mineralization: a contouring method for targeting in gold exploration, J. Struct. Geol., 26, 1087–1108, 2004.

Turcotte, D. L. and Schubert, G.: Geodynamics, Cambridge university press, 2002.

Vallis, G. K.: Atmospheric and oceanic fluid dynamics, Cambridge University Press, 2017.

Woods, A. W.: Flow in porous rocks, Cambridge University Press, 2015.